Femtosecond Transient Absorption Microscopy of Singlet Exciton Motion in Side-Chain Engineered Perylene-Diimide Thin Films

Raj Pandya[†], Richard Y.S. Chen[†], Qifei Gu[†], Jeffrey Gorman[†], Florian Auras[†], Jooyoung Sung[†], Richard Friend[†], Philipp Kukura[‡], Akshay Rao[,†], Christoph Schnedermann*[,†]*

[†] Department of Physics, Cavendish Laboratory, University of Cambridge, JJ Thomson Avenue, Cambridge, CB3 0HE, U.K.

[‡] Physical and Theoretical Chemistry Laboratory, Oxford University, South Parks Road, Oxford OX1 3QZ, U.K.

Abstract

We present a statistical analysis of femtosecond transient absorption microscopy applied to four different organic semiconductor thin films based on perylene-diimide (PDI). We achieve a temporal resolution of 12 fs with simultaneous sub-10 nm spatial precision, which enables us to directly probe the underlying exciton transport characteristics within 3 ps after photoexcitation free of model assumptions. Our study reveals sub-picosecond coherent exciton transport (12 – 45 $cm^2\ s^{-1}$) followed by a diffusive phase of exciton transport (3 – 17 $cm^2\ s^{-1}$). A comparison between the different films suggests that the exciton transport in the studied materials is intricately linked to their nanoscale morphology, with PDI films that form crystalline films with large domain sizes exhibiting the largest diffusion coefficients and transport lengths. Our study demonstrates the advantages of directly studying ultrafast transport properties at the nanometer length scale and highlights the need to examine nanoscale morphology when investigating exciton transport in organic as well as inorganic semiconductors.

Introduction.

Organic semiconductors are of interest for a large variety of light-emitting[1,2] and light-harvesting applications[3,4]. These materials can be readily synthesized, easily integrated into devices[5], display a high degree of electronic tunability[6] and have high absorption cross-sections[7]. In contrast to inorganic semiconductor materials, however, photoexcitation of organic semiconductors results in strongly-bound electron-hole pairs (excitons).[8] Understanding the spatio-temporal behavior of excitons is thus important both from a fundamental point of view and also to further improve device functionality.

A challenge associated with determining exciton transport properties arises from their intrinsically short lifetimes, which are typically on the femto- to picosecond time scales. Ultrafast pump-probe spectroscopy has been used to measure exciton diffusion lengths in a wide variety of organic and inorganic materials, with transport lengths of up to 1 μm reported in some cases[9–15]. Such studies, however, require careful modelling of the observed photo-response which involves several approximations that can greatly affect the extracted transport parameters. Additionally, ensemble-level spectroscopic studies average out the effect of micro-morphologies due to the large sample volume probed simultaneously, further complicating accurate modelling of the transport parameters.[16–18]

In this context, transient absorption microscopy enables local probing of photo-induced dynamics in materials, thereby avoiding some of the key challenges associated with the determination of transport parameters encountered in ensemble-based spectroscopic approaches. The time-resolution of current transient absorption microscopy setups, however, is typically

restricted to ~100 – 200 fs, preventing direct insight into the ultrafast dynamics occurring directly after photo-excitation[19–25]. To overcome this shortcoming, we have recently developed an ultrafast extension of transient absorption microscopy, which can access sub-100 fs exciton transport behavior in real time and space.[26–28]

Here, we discuss the different implementations of transient absorption microscopy and apply this technique to four different thin film organic semiconductor films based on perylene-diimide (PDI) molecules with varying side groups. PDIs are one of the most intensely studied class of organic semiconductor materials owing to their high degree of chemical tunability, environmental stability and ability to readily form highly organized supramolecular structures *via* wet and dry processing methods[29–33]. PDIs have found use in a range of applications from n-type transistors[34], high efficiency organic photo-voltaic cells as replacements for fullerenes[35,36] and more disparate technologies such as gas sensors[37] and dye lasers[38,39]. In this work, we study evaporated PDI films and show that the crystallinity of PDI thin films controls the singlet exciton transport behavior during the initial sub-3 ps excited-state relaxation. Measurement of several sample locations across the homogenous films unexpectedly shows a large variation in the transient absorption kinetics which are not correlated to the exciton transport properties. Instead, we find irrespective of the kinetics that each (crystalline) film features two distinct spatial expansion regimes within the first 3 ps after photo-excitation: An initial, sub-500 fs expansion with associated diffusion coefficients reaching 12 – 45 $cm^2\ s^{-1}$, which is followed by a slower expansion with diffusion coefficients of 3 – 17 $cm^2\ s^{-1}$. Our study provides a systematic investigation into exciton transport in PDI films and how this can be influenced by the molecular packing and crystallinity. More generally our results

highlight the importance of microscopic structure on energy transport in organic semiconductor materials.

Methods.

Materials. The syntheses of **PDI 1**, **PDI 3** and **PDI 4** were adapted from Yang *et al*.[40]

PDI 1. A reaction mixture containing perylene-3,4,9,10-tetracarboxylic dianhydride (3.14 g, 8.00 mmol, 1.0 eq.), *n*-butylamine (1.76 g, 24.0 mmol, 3.0 eq.) and 45 g imidazole was heated under argon at 160 °C for 3 h. Chlorobenzene (30 mL) was added while the mixture was still hot and the resulting suspension was slowly added into 2 M aqueous HCl. The solids were collected by filtration, washed with H2O, MeOH and acetone, and re-dispersed in 200 mL chloroform/acetone (1:1 *v/v*). After stirring overnight, the solids were collected by filtration, washed successively with H_2O, acetone, $CHCl_3$ (20 mL), and Et_2O, and dried under high vacuum to yield the title compound as deep purple microcrystalline needles (3.98 g, 7.92 mmol, 99%).

^{1}H NMR (400 MHz, $CDCl_3$) δ 8.71 (d, J = 8.0 Hz, 4H), 8.65 (d, J = 8.1 Hz, 4H), 4.26 – 4.20 (m, 4H), 1.81 – 1.72 (m, 4H), 1.53 – 1.43 (m, 4H), 1.01 (t, J = 7.4 Hz, 6H).

PDI 2. A reaction mixture containing perylene-3,4,9,10-tetracarboxylic dianhydride (392 mg, 1.00 mmol, 1.0 eq.), cyclohexylamine (397 mg, 4.0 mmol, 4.0 eq.), $Zn(OAc)_2$ x $2H_2O$ (220 mg, 1.00 mmol, 1.0 eq.), and 8 g imidazole was heated under argon at 130 °C for 16 h. Chlorobenzene (30 mL) was added while the mixture was still hot, and the resulting suspension was slowly added into 2M aqueous HCl. The solids were collected by filtration, washed with H_2O, MeOH and acetone, re-dissolved in a $CHCl_3$/EtOAc (95:5 *v/v*) mixture (2 L), and passed through a plug of silica gel. All volatiles were removed under reduced pressure. The solid residue was dissolved in 600 mL

$CHCl_3$ at 95 °C, layered with EtOAc (400 mL) and left to crystallize over 3d. The precipitate was separated by filtration, washed with a small amount of $CHCl_3$ and dried under high vacuum to yield the title compound as a red fibrous solid (600 mg, 0.901 mmol, 90%).

^{1}H NMR (500 MHz, $CDCl_3$) δ 8.67 (d, J = 8.0 Hz, 4H), 8.61 (d, J = 8.0 Hz, 4H), 5.05 (tt, J = 12.2, 3.8 Hz; 2H), 2.62 – 2.53 (m, 4H), 1.94 – 1.91 (m, 4H), 1.80 – 1.73 (m, 6H), 1.50 – 1.33 (m, 6H).

PDI 3. Synthesized using the same procedure as described for **PDI 1**, but using *n*-octylamine (87% yield).

PDI 4. A reaction mixture containing perylene-3,4,9,10-tetracarboxylic dianhydride (1.96 g, 5.00 mmol, 1.0 eq.), 3-pentylamine (1.74 g, 20.0 mmol, 4.0 eq.) and 28 g imidazole was heated under argon at 160 °C for 4 h. Chlorobenzene (30 mL) was added while the mixture was still hot, and the resulting solution was slowly added into 2 M aqueous HCl. The mixture was extracted with $CHCl_3$, and the organic phase was dried over $MgSO_4$ and concentrated under reduced pressure. Purification by column chromatography (silica gel, DCM) yielded the title compound as a red crystalline solid (2.31 g, 4.35 mmol, 87%).

^{1}H NMR (400 MHz, $CDCl_3$) δ 8.63 (d, J = 7.9 Hz, 4H), 8.55 (d, J = 8.1 Hz, 4H), 5.07 (tt, J = 9.5, 5.9 Hz, 2H), 2.34 – 2.20 (m, 4H), 2.02 – 1.89 (m, 4H), 0.94 (t, J = 7.4 Hz, 12H).

Evaporation. The freshly synthesized PDI was transferred to an evaporator chamber and kept at 150°C overnight under high vacuum (< 10^{-6} mbar) to remove any residual solvent prior to thermal evaporation. A 145-nm thick layer of PDI was thermally evaporated at a rate of 0.5 ± 0.1 Å s^{-1}.

The rate was monitored using a standard Quartz-crystal microbalance and calibrated with atomic force microscopy measurements.

Film characterization. XRD was performed using a Bruker X-ray D8 Advance diffractometer with Cu Kα1,2 radiation (λ = 1.541 Å). Spectra were collected with an angular range of $2° < 2\theta < 20°$ and $\Delta\theta = 0.01431°$ over 60 min. Measurements were made on evaporated films pre-cleaned silicon substrates. Atomic force microscopy (AFM) measurements were done in tapping mode (Veeco Dimension™ 3100) at room temperature. The AFM cantilever was provided by MikroMasch. The tip radius was about 10 nm.

Femtosecond transient absorption microscopy. The femtosecond wide-field detected transient absorption microscope has been described in detail previously.[26,27] Briefly, a Yb:KGW amplifier system (LightConversion, Pharos, 5 W, 180 fs, 1030 nm, 200 kHz) was used to seed two white-light stages for pump and probe generation. The pump white-light (3 mm Sapphire) was spectrally adjusted with a 650 nm short-pass filter (FESH650, Thorlabs), and compressed to 10 fs for all optical elements with two pairs of third-order compensated chirped mirrors and a wedge-prism pair (Layertec). Subsequently, the mode of the pump pulse is cleaned by a pinhole before being focused through the objective lens (NA = 1.1, oil immersion) to a spot size of ~260 nm (full-width-half-maximum). The probe white-light (3 mm YAG) was spectrally adjusted to 650 – 900 nm in a home-build fused silica prism filter and compressed to 7 fs with a pair of third-order compensated chirped mirrors and a wedge-prism pair (Venteon) before being free-space focused onto the sample (20 micron Gaussian spot size full-width-half-maximum). The transmitted probe was imaged onto an emCCD (Rolera Thunder, Photometrics) at 55.5 nm/pixel as verified by a resolution target. The

frame rate of the camera was set to 30 Hz with an integration time of 11 ms and pump off/on images were generated by a mechanical chopper at a frequency of 15 Hz. For the measurements, we adjusted the pump fluence to achieve initial carrier concentrations (n_0) in the range: $n_0 = 1.02 \times 10^{17} - 2.19 \times 10^{18}$ cm^{-3} for all films (see supporting information, section 2 for further details).

Results.

Design criteria for an ultrafast transient absorption microscope

Recently, several groups have combined optical pump-probe spectroscopy schemes with microscopic detection modalities to correlate spatial and dynamic material parameters[41]. These experiments generate a spatially localized excited-state population by tightly focusing an optical pump pulse onto the sample by means of a high numerical aperture (NA) microscope objective. This results in a diffraction-limited excitation spot in the form of a two-dimensional Gaussian function, with a standard deviation, σ, given by the Abbe criterion:

$$\sigma = \frac{1}{2\sqrt{2\ln(2)}} \frac{\lambda}{2\,\mathrm{NA}} \qquad (1)$$

Where λ is the pump wavelength. Subsequently, a time-delayed, diffraction-limited probe pulse is delivered to the sample by the same objective and its transmission collected with a second objective before it is detected with a photo-diode coupled to a lock-in amplifier (synced to the pump pulse modulation, Figure 1a). The transient absorption image for a given probe wavelength and time delay is constructed by slow point-scanning of the probe over the excitation region, producing a two-dimensional Gaussian transient point-spread function (Figure 1b,c). This detection is thus comparable to a confocal microscope but without the use of a confocal pinhole.

An important consequence of recording transient absorption images as a function of time delay is that the achievable spatial accuracy, *i.e.* the ability to distinguish different spatial profiles, is determined solely by the signal-to-noise ratio. Owing to the extremely sensitive lock-in detection with avalanche photo-diodes (noise floor of down to 10^{-7}), these microscopes routinely achieve a spatial precision of $\sigma \sim 10 - 50$ nm and have been successfully utilized to reveal charge-carrier

dynamics with direct access to spatial domains in thin film inorganic and organic semiconductors. Yet, the temporal resolution achieved in these systems is typically limited to >100 fs, preventing a direct visualization of the initial exciton diffusion processes for most systems. In addition, the construction of a transmission microscope featuring two high-NA objectives is technically challenging and must be carried out carefully to avoid possible imaging artefacts. These constraints can, however, be mediated by operating the microscope in reflection, which requires only a single objective.

To explore ultrafast exciton dynamics at sub-100 fs time scales, we have recently developed an ultrafast optical transient absorption and reflection microscope, which can achieve a time resolution of 12 fs together with a spatial precision of $\sigma < 10$ nm. We replaced the probe point scanning and lock-in detection with free-space illumination and wide-field imaging with a high-sensitivity emCCD camera (Figure 1d). Consequently, probe pulses no longer experience the high degree of temporal dispersion arising from the illumination, which allows for straightforward probe compression down to 7 fs at the sample with commercial optical elements. The transmitted probe pulses are imaged using a low-dispersion oil-immersion objective (NA = 1.1), which is simultaneously used to deliver the diffraction-limited pump pulses to the sample (Figure 1e). This low dispersion objective is critical to achieve a near transform-limited temporal compression of the pump pulses to 10 fs with commercial optical elements, resulting in an effective time resolution of the experiment of 12 fs. It is important to note that our objective achieves its low dispersion by lacking chromatic aberration and flat field correction lenses, resulting in an overall imaging quality which deteriorates over a large field of view. However, the differential point-spread function in a transient absorption microscope is only weakly affected by the imaging objective in a small field

of view (2 – 3 µm), if detection is carried out with a sufficiently narrow-band pass filter in front of the detector.

An important difference of our wide-field imaging detection compared to a confocal-like microscope is the intrinsic shape of the point spread functions. Photo-excitation by a diffraction-limited, two-dimensional Gaussian pump pulse, generates a spatially-localized perturbation of the dielectric function of the material, which can be represented by a two-dimensional Gaussian-shaped aperture. The resulting far-field radiation pattern of a transmitted plane-wave probe pulse consequently exhibits a Fraunhofer diffraction pattern also known as Airy disk (or Bessel function of the first kind) arising from the interference of light detected from different sample regions (Figure 1f). This interference effect is preserved over the intrinsic coherence length, L_{coh}, of the employed probe pulses, which can be approximated from its spectral linewidth by

$$L_{\mathrm{coh}} = \frac{c}{\pi \, \Delta\upsilon} \quad (2)$$

where c is the speed of light and $\Delta\upsilon$ the bandwidth of the pulse. For a 7 fs probe pulse centered at 800 nm, we obtain a coherence length of $L_{\mathrm{coh}} \approx 700$ nm. Based on this value and the NA of our objective, we universally expect to observe a pronounced first diffraction ring in our imaging apparatus, deviating from the pure two-dimensional Gaussian point-spread function obtained in confocal-like imaging (compare Figure 1c,f).

The spatial accuracy of our apparatus is determined in the same way by the signal-to-noise ratio of the transient point-spread function. This can optimized by adjusting the image magnification to enable maximum light collection for each single pixel of the detector, resulting in a typical noise-level of 10^{-5}. While this is 2 orders of magnitude worse than a lock-in detection scheme, the full

image collection allows us to efficiently reference for laser noise and is thus shot-noise limited to well below this value, eliminating the need for highly stable laser sources or fast pump modulation. A wide-field illumination and detection scheme furthermore removes the need to physically scan the probe pulses over the sample, preventing potential scanning or degradation artefacts. Lastly, organic semiconductors often display high exciton absorption cross-section resulting in high signal-to-noise ratios even in the linear excitation regime, enabling a spatial accuracy of $\sigma < 10$ nm for most materials. We highlight, that the same accuracy is possible to attain in a confocal-like microscope implementation.

Spatio-temporal singlet exciton dynamics in PDI films

Steady-state measurements. Films of the four different PDIs (**PDI 1 – 4**) were prepared by thermal evaporation under identical preparation conditions (Figure 2a). The absorption spectra of the different PDI thin films display a broad visible absorption feature between 400 – 650 nm with distorted vibronic progressions, in agreement with previous studies (Figure 2b). The lowered intensity ratio of the first two vibronic peaks in the absorption spectra of **PDI 1 – 4** compared to the isolated monomer in solution is a strong indicative of H-aggregate formation.[42,43] In PDI aggregates/films, the alignment of the molecular transition dipoles (head-to-tail or side-by-side) and hence long-range Columbic interactions between PDI chromophores dominate the overall shape of the absorption spectrum. Nonetheless, small displacements between nearest-neighbour PDIs can induce subtle changes in the absorption spectra that critically affect the excited-state photo-dynamics of PDI aggregates/films. As shown in Figure 2b, the non-negligible low-energy absorption bands reflect not only a significant deviation in the intermolecular packing geometry from the perfect H-type geometry, but reveal additionally the existence of short-range interactions,

which arise from Frenkel/Charge-transfer state mixing. As outlined in other studies[44,45], short-range charge-resonance interactions can be either H-like or J-like depending on the degree of lateral spatial offset[46], which is dictated by the nodal positions of neighbouring frontier molecular orbital overlap.[47] Accordingly, the presence of additional H- and J-like features in **PDI 1 – 4** thin films implies a complex nature of excited-state dynamics originating from complex short- and long-range molecular interactions.

Although the molecular packing dictates the absorption spectra of the measured films, a spectral analysis alone is insufficient to provide a complete picture of the long-range molecular ordering in PDI thin films. We therefore conducted additional X-ray diffraction measurements to gain insight into the degree of crystallinity (Figure 2c). We find that **PDI 1** lacks pronounced discernible features indicative of an amorphous packing arrangement, while **PDI 2**, **PDI 3** and **PDI 4** display crystalline structures with longer-range order. A semi-quantitative analysis of the crystalline domain size can be obtained *via* atomic force microscopy (supporting information, section 1) which confirms that the average grain sizes in our films increase from **PDI 1** (amorphous) with sub-30 nm domains to **PDI 4** (quasi single-crystalline) with micron-sized domains. By comparison, **PDI 2** and **PDI 3** show similar intermediate domain sizes of ~120 nm, despite exhibiting different molecular packing based on X-ray diffraction. We remark, that the width of the X-ray peaks for all films approaches the instrument response limit (see supporting information, section 5) precluding analysis using the Scherrer broadening equation. We note that in the case of **PDI 4**, the individual $K\alpha_1$ and $K\alpha_2$ peaks can be resolved as a split peak in the lowest angle reflection $2\theta = 4.56$ (Figure 1c, green curve), indicating a highly ordered film.

Femtosecond transient absorption microscopy. The qualitative trend in crystallinity without significant changes in the absorption spectrum allows us to directly investigate the effect of local morphology on the underlying transport behavior of photo-excited excitons in these materials. To deduce the transport parameters directly after photo-excitation, we carried out femtosecond wide-field detected transient absorption microscopy employing a diffraction-limited 10 fs visible pump pulse (σ = 112 nm) centered at 560 nm in combination with a time-delayed, 7 fs wide-field probe pulse ($\sigma \sim 10$ µm) centered at 800 nm (Figure 1d-f). We subsequently recorded the transient spatio-temporal photo-dynamics at 740 nm. This probe wavelength is associated with a broad photo-induced absorption band which is attributed to singlet excitons and thus allows direct insight into the excitonic transport behavior of this class of materials. We remark that no additional excited-state signatures are present at this probe wavelength[43] and that the samples show only a small degree of surface roughness (~1-2 nm).

To gain insight into the spatio-temporal exciton diffusion, we model the initial pump-induced population at $t = t_0$ as

$$n_0(x, y, t_0) = N \exp\left(-\frac{(x-x_0)^2+(y-y_0)^2}{2\,\sigma(t_0)^2}\right) \qquad (3)$$

Assuming carrier transport with a constant diffusion coefficient, D, in the absence of exciton-exciton annihilation, we can construct the associated differential diffusion equation

$$\frac{\partial n(x,t)}{\partial t} = D\left[\frac{\partial^2 n(x,t)}{\partial x^2}\right] - \frac{n(x,t)}{\tau} \qquad (4)$$

which allows us to describe the spatial profile of the exciton population at a given time delay, t, as

$$n(x, y, t) = N \exp\left(-\frac{(x-x_0)^2+(y-y_0)^2}{2\,\sigma(t)^2}\right) \qquad (5)$$

we note that the measurements presented in this study show no pronounced differences in their spatial dynamics under different initial carrier concentrations (supporting information, section 2;

initial carrier concentration (n_0) in all measurements range from $n_0 = 1.02 \times 10^{17} – 2.19 \times 10^{18}$ cm^{-3}). We can consequently neglect higher order carrier annihilation terms in Equation 4.[48] The time-dependent spatial profiles of the measured transient point-spread functions, as measured by σ, are then related to the underlying transport behavior via

$$\mathrm{MSD}(t) = \sigma(t)^2 - \sigma(t_0)^2 = 2\,D\,(t - t_0) \qquad (6)$$

where MSD denotes the mean-square displacement. Equation 6 can be extended to include a non-linear time dependence via

$$\mathrm{MSD}(t) = \sigma(t)^2 - \sigma(t_0)^2 = B\,(t - t_0)^{\alpha} \qquad (7)$$

in which B is an arbitrary scaling factor and α accounts for non-linearity in time. In the case of $\alpha = 1$ we retrieve normal diffusion, while $\alpha > 1$ is known as super-diffusive behavior and $\alpha < 1$ is referred to as sub-diffusive behavior.

The transient absorption images obtained for our films features a near isotropic point-spread function with a negative differential transmittance signal at its center, as expected for a photo-induced absorption signal induced by a Gaussian excitation spot (see supplementary information, section 3 for detailed discussion). In addition, we observe a first positive diffraction ring as expected in wide-field microscopy and in agreement with previous studies. We note that the slight asymmetry in the point-spread function is due to the imperfect imaging conditions of our objective. Critically, however, this asymmetry does not translate to the central portion of the point-spread function.

Following Equation 5, we describe the transient point-spread function at each time delay with a two-dimensional Gaussian function:

$$G(x, y) = A \exp\left(-\frac{(x-x_0)^2}{2\sigma_x^2} - \frac{(y-y_0)^2}{2\sigma_y^2}\right) + \mathrm{offset} \qquad (8)$$

where x_0 and y_0 are the center-of-mass coordinates of the Gaussian function and σ_x and σ_y the associated standard deviations. Equation (8) allows us to retrieve time-dependent dynamics encoded in *A* as well as the spatial profile given by the standard deviations σ_x and σ_y. To compare the transient point-spread functions of all PDI films, we focus in this work exclusively on the temporal evolution of the mean spatial profile given by $\sigma = \frac{\sigma_x + \sigma_y}{2}$ (see supplementary information, section 3 for a discussion on the asymmetry of the transient point-spread function).

The time-dependent dynamics, represented by *A*, exhibit for all films an instrument-response limited signal rise (~12 fs) followed by a decay within the first 3 ps that can be adequately described with two exponential time constants (Figure 3, top). These bi-exponential decay dynamics are preserved at different sample locations for all films (differently colored lines in Figure 3), but the initial, fully-resolved decay component exhibits a noticeable spread which is most pronounced for **PDI 3** (915 ± 450 fs (49%)) followed by **PDI 4** (576 ± 189 fs (33%)) and **PDI 2** (619 ± 142 fs (23%)). **PDI 1** (829 ± 154 fs (19%)) on the other hand shows the smallest spread in the initial dynamics. We remark that in contrast to transient absorption spectroscopy, the dynamics retrieved in transient absorption microscopy (*A* in Equation 8) are a superposition of spatially-localized exciton decay and additional decay contributions arising from diffusive transport.

To assess the degree of spatial dynamics, we extracted the average time-dependent standard deviations from Equation 1 (Figure 3, middle panel). The transient point-spread function for **PDI 1** measured 50 fs after photo-excitation shows an average standard deviation of σ = 147 ± 8 nm, which is in excellent agreement with the expected diffraction limit at a probe wavelength of 740

nm (σ = 143 nm). In contrast, the initial point-spread function for **PDI 2**, **PDI 3** and **PDI 4** reaches spatial standard deviation values of σ = 191 ± 4, 175 ± 14 and 161 ± 10 nm. Which are all slightly above the expected diffraction limit reached for **PDI 1**. We attribute this increase to the effect of spherical aberrations, which are more pronounced in crystalline domains due to enhanced inter-molecular coupling.[49] Between 50 fs and 3 ps, we observe no pronounced change in the spatial dynamics for **PDI 1**, despite a ~50% decrease in signal intensity over the same interval (Figure 3a, middle and top panel, respectively). By comparison, **PDI 2**, **PDI 3** and **PDI 4** all undergo spatial broadening over time (Figure 3b-d, middle panel) with average standard deviation changes of Δσ = 9.7 ± 1.5 and 11.5 ± 1.7 nm for **PDI 2** and **PDI 3** within 3 ps, and Δσ = 21.7 ± 5.4 nm for **PDI 4** within 1.5 ps after photo-excitation. The observed spatial dynamics are largely independent of the probed sample position with more variation observed for **PDI 4**.

To extract the actual diffusion transport behavior for the studied films, we computed the corresponding time-dependent MSD curves according to Equation 6 with respect to t = 50 fs (Figure 3, bottom panel). This time delay was selected to avoid parasitic coherent artefact contributions at t = 0 ± 50 fs, which can be pronounced in all ultrafast transient absorption measurements with sub-20 fs pulses and wavelength-resolved detection (see e.g. Figure 3d, middle panel, sub-50 fs behavior). The MSD curve for **PDI 1** shows no expansion above our noise level irrespective of the sample position (Figure 3a, bottom, differently colored lines), suggesting vanishingly small diffusion in this film during the first 3 ps after photo-excitation. Upon describing the MSD curve in **PDI 1** with a linear fit (Equation 6) and calculating the statistical variation between different sample position, we can extract the error range of the retrieved diffusion coefficients in our setup to be ± 0.07 cm^2 s^{-1}. **PDI 2**, **PDI 3** and **PDI 4** in contrast show a

pronounced increase in their MSD over time for all measured sample positions (Figure 3b-d, bottom) with maximum MSD values of 3815 ± 606 and 4217 ± 599 nm^2 for **PDI 2** and **PDI 3** in the first 3 ps, and 8146 ± 2343 nm^2 for **PDI 4** within 1.5 ps after photo-excitation.

Discussion

A comparison of the absorption spectra for all measured films suggests that the exciton bandwidth for each of the PDI films is similar[50], whereas morphology characterization (X-ray and AFM) reveals differences in the degree of crystallinity. Among the investigated films, **PDI 1** exhibits an amorphous crystal packing which causes high site energy differences and an elevated trap state density (grain boundaries and point-defects). Following photo-excitation of **PDI 1** (Figure 3a), the initially delocalized exciton will get rapidly trapped locally and decay due to the high trap state density imposed by the amorphous crystal packing. Since the fast decay component observed in **PDI 1** (829 fs, Figure 4a) is independent of the probed location in the film, we assign it to trap kinetics, largely free of diffusive contribution. We hence suggest that spatial transport of excitons in **PDI 1** is consequently subject to large activation barriers and thereby restricted to diffusive hopping (incoherent transfer) between amorphous sites arising from slow de-trapping kinetics on time scales exceeding our time window (Figure 3a, top). Thus, **PDI 1** serves as an ideal control system for the spatio-temporal dynamics of the other studied films. We remark that in the initial 3 ps after photo-excitation neither intersystem crossing nor singlet fission have been reported to occur in PDI films and we can be confident that we probe the population of singlet excitons.[43,51]

PDI 2, **PDI 3** and **PDI 4** all exhibit long-range order, as evident from the X-ray diffraction patterns shown in Figure 2c. We can garner an estimate of the grain sizes from AFM of ~120 nm for **PDI 2** and **PDI 3** and micron-sized domains in **PDI 4**. In these crystalline domains, the coupling strength between adjacent PDI molecules are expected be higher than the site-to-site energy difference, rendering spatial exciton transport kinetics competitive with local trap kinetics. To assess the similarity in initial decay dynamics for these films, we employ a statistical analysis based on a two-tailed Student *t*-test by taking into account all measured data sets (sample size ≥ 6, Figure 4a). This statistical test allows to quantify the difference in means of two different data sets and is frequently employed to estimate if two data sets are identical or different within a given significance-level (*p-value*). Based on a significance level of $p < 0.05$, we deduce that **PDI 2**, **PDI 3** and **PDI 4** show statistically identical lifetimes that are significantly different from **PDI 1**. We note that **PDI 3** weakens this assignment marginally due to its large variation in lifetimes (49% standard deviation), but the significant difference to **PDI 2** and **PDI 4** is interpreted as sufficient to differentiate **PDI 1** from all other films. Since the initial photo-dynamics in **PDI 1** are solely related to trap kinetics and show no spatial transport, we conclude that the decay dynamics in **PDI 2, PDI 3** and **PDI 4** arise due to significant contributions from spatial exciton transport.

The spatial dynamics (Figure 3b-d, bottom panel) appear on first glance sub-linear over the investigated time-window, which is indicative of hop-diffusive motion as described by Equation 7. We were, however, unable to satisfactorily describe the spatial dynamics with a sub-linear diffusion fit over the full time window (see supporting information, section 4), and therefore opted to describe the MSD curves by two linear diffusion segments to extract the associated diffusion coefficients, D. For **PDI 2** and **PDI 3** we used time segments from 50 – 800 fs (D_1) and from 1.2

– 3 ps (D_2), while **PDI 4** required a different segmentation from 50 – 450 fs (D_1) and 0.85 – 1.50 ps (D_2). Applying Equation 6 to each segment results in two satisfactory fits with average diffusion coefficients of: D_1(**PDI 2**) = 11.9 ± 1.5 $cm^2\ s^{-1}$, D_2(**PDI 2**) = 3.2 ± 0.3 $cm^2\ s^{-1}$; D_1(**PDI 3**) = 13.9 ± 2.7 $cm^2\ s^{-1}$, D_2(**PDI 3**) = 3.3 ± 0.6 $cm^2\ s^{-1}$; D_1(**PDI 4**) = 45.3 ± 17.6 $cm^2\ s^{-1}$, D_2(**PDI 4**) = 17.3 ± 4.1 $cm^2\ s^{-1}$ (Figure 4b,c). We note that we observe in all PDIs a relatively large variation in the retrieved kinetics which are dependent on the sample location, but only a small variation in the diffusion parameters. This suggests that transport parameters extracted solely from lifetimes can lead to substantial errors in understanding exciton transport in PDI films.

A statistical analysis based on a Student *t*-test suggests that the retrieved diffusion coefficients in both time segments are similar only between **PDI 2** and **PDI 3** ($p_1 = 0.11$, $p_2 = 0.87$), while **PDI 4** displays significantly higher diffusion coefficients ($p_{1,2} < 0.01$) albeit with a much larger internal variation. These values demonstrate that exciton diffusion is similar in **PDI 2** and **PDI 3** but significantly higher in **PDI 4**. Qualitatively, this trend mirrors the average grain size distribution (supporting information, section 1) where **PDI 2** and **PDI 3** exhibit similar sub-diffraction limited domains (~120 nm), whereas **PDI 4** features micron-sized domains which exceed the diffraction limit.

It is interesting to note that **PDI 2** and **PDI 3** show statistically identical diffusion coefficients, despite exhibiting different X-ray diffraction patterns, *i.e.* molecular packing order. On the other hand, **PDI 4** displays markedly higher diffusion coefficients, while showing similar long-range order as **PDI 2** and **PDI 3** in X-ray diffraction measurements. Exciton diffusion in PDI films therefore appears to be mainly limited by the microscopic grain size[52]. In this case the higher

diffusion coefficients for **PDI 4** can be understood as a consequence of a lower trap state density, achieved by removing grain boundaries. Additionally, a higher crystallographic order as suggested from AFM in **PDI 4** further avoids additional intra-grain point defects. It is important to stress that the spatial resolution in fs-TAM is diffraction limited to the probe wavelength of interest and corresponds to σ = 143 nm, or a full-width-half-maximum of 336 nm. This implies that our observations relate to photo-excitation of several domains in **PDI 2** and **PDI 3** and the extracted diffusion coefficients thus sensitively monitor the micro-structure of our evaporated PDI films.

The magnitude of the diffusion coefficients extracted from the second time segment is similar to previous reports for highly mobile singlet excitons in organic semiconductors.[19,53] By contrast, the first time segment exceeds values of normal diffusive transport. For molecular aggregates, the initial exciton dynamics are governed by an interplay between the coupling strength of adjacent PDI molecules (J) and the energetic disorder (ΔE_n)[54]. If the interaction strength and the site-to-site energy differences are comparable, exciton energy transfer falls into an intermediate regime between coherent (wavelike) to incoherent (hopping) mechanisms[55]. An analysis of the absorption spectra reveals that all films investigated here belong to an intermediate coupling regime ($J \sim 600$ cm^{-1}).[56] The exciton transfer dynamics are thus neither in the strong- or weak coupling regime and can be controlled by the site-to-site energy difference (energetic disorder), *i.e.* the long-range molecular ordering. Since the initial ultrafast spatial dynamics are only observed for crystalline films, we attribute the early spatial expansion to coherent exciton migration. Intriguingly, the time scale for this process (sub-500 fs) aligns well with previously reported studies on exciton transport in molecular oligomers,[56] further supporting our assignment. We stress that, while we extracted the diffusion coefficients for the different time segments with a normal diffusion equation analysis,

the observed spatial dynamics in the first ~500 fs after photo-excitation should not be interpreted as normal, random-walk diffusive behavior. Our analysis, instead serves as a benchmarking tool to compare critical diffusion parameters among different systems and time scales. More detailed modelling studies are required to in-detail understand coherent exciton migration in femtosecond transient absorption microscopy.

In addition to the diffusion coefficient, it is important to benchmark the exciton transport length, L, according to Equation 9.

$$L = \sqrt{2D\,\tau} \quad (9)$$

where τ denotes the lifetime of the underlying process. Equation 9 can be applied if the spatial expansion is fully resolved, allowing us to extract the coherent exciton migration transport lengths (L_1) from the first time segment. We note that lifetime, τ, in Equation 9 refers to the intrinsic coherent exciton lifetime, which is different from the apparent lifetime extracted in Figure 4a which includes diffusion-mediated decay pathways. While the exact determination of the coherent exciton lifetime for the studied PDI films is beyond the scope of this study, we can nonetheless estimate a lower lifetime on the order of τ ~ 100 fs based on the overall length of the time segment as well as from previous studies in PDI oligomers[56]. The associated diffusion length, L_1, corresponding to ultrafast coherent exciton diffusion based on the average diffusion coefficient then computes to 15.4 ± 1.0, 16.6 ± 1.6 and 30.1 ± 5.8 nm for **PDI 2**, **PDI 3** and **PDI 4**, respectively.

Based on these results (overview in Table 1), we can identify key factors affecting the exciton transport data of the PDI films investigated in this study and organic semiconductor materials in general. A critical aspect observed here is that PDI films have to show a minimum degree of long-

range molecular packing to ensure exciton propagation, which can be qualitatively assessed with X-ray diffraction measurements. As expected, highly amorphous films will not display significant exciton transport. Provided the samples display sufficient crystallinity, the degree of crystallinity appears to have only a weak effect on the overall transport behavior provided the long-range coupling mechanisms are similar, which can be deduced by comparing absorption spectra of relevant films. Critically, large diffusion coefficients, and therefore transport lengths are best achieved by operating in a coherent exciton transport regime (sub-500 fs), which is ensured by maximizing the domain sizes and crystal packing of the films to suppress trap states (such as grain boundaries and point defects) as much as possible.

Conclusion.

In summary, we have demonstrated femtosecond transient absorption microscopy on four side-chain engineered PDI thin films and extracted their transport properties. By carefully considering the micro-structure of the grains and the inherent crystallinity, we identified two transport regimes occurring on the sub-3 ps time scale. A first regime takes place within ~500 fs after photo-excitation and is governed by coherent exciton transport, followed by a second regime characterized by normal diffusion of highly mobile excitons. Our results demonstrate that crystallinity and domain size are critical elements in achieving high exciton diffusion coefficients, with crystalline films where the domain size is large (>1 μm) performing best. This makes it possible to optimize organic semiconductors such as PDIs by carefully engineering the involved side chains to optimize the grain size and crystal packing and will be of particular relevance for organic photo-voltaic technology where the exciton diffusion length is a key parameter for device optimization.

More generally our approach highlights the potential of femtosecond transient absorption microscopy for imaging carrier transport in materials in the coherent exciton diffusion regime. Since the photo-excited signals obtained in our measurements are directly proportional to carrier population the technique provides a useful complement to photo-luminescence[9] based methods without potential drawbacks of photon-waveguiding[57], *etc*. More importantly this method can be applied to non-luminescent materials and for tracking the motion of a range of different quasi-particles (plasmons, charges, phonons, polaritons, *etc*) in organic and inorganic materials. The high time resolution achieved in these experiments will allow for the tracking of electronic population on the timescales of electronic dephasing providing insight to a hitherto unexplored regime of quasi-particle dynamics.

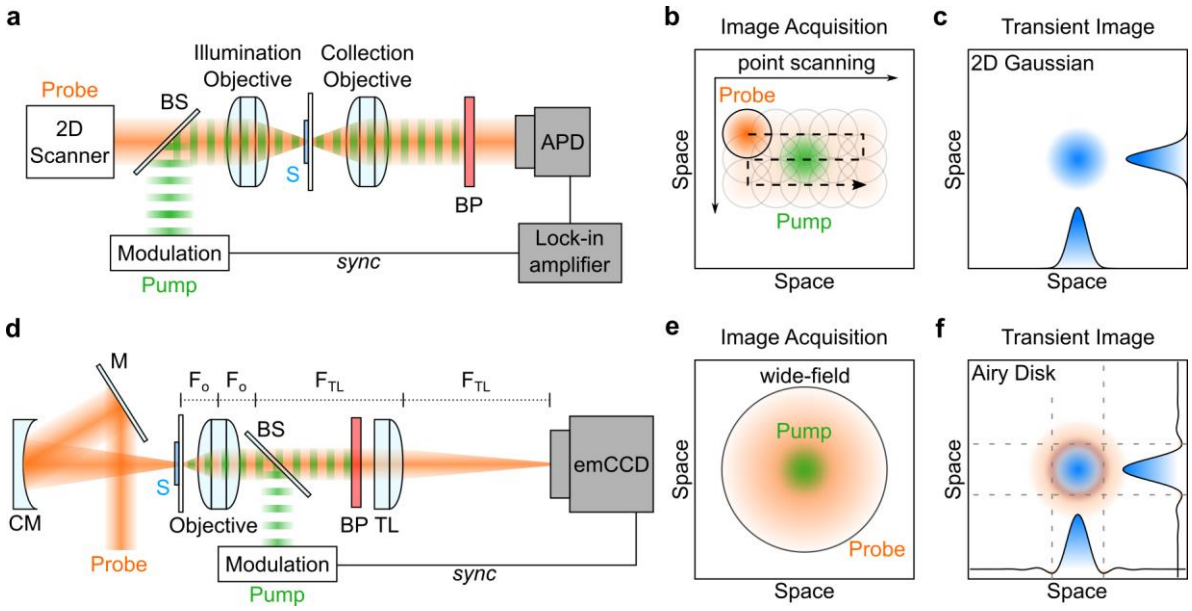

Figure 1. Implementations of transient absorption microscopy. **a-c**. Confocal-like microscopy based on point-scanning and high-sensitivity point detection with an avalanche photodiode (APD). **d-f**. Wide-field microscopy based on free-space probe focusing and two-dimensional image detection. BS – beam splitter, S – sample, BP – band pass filter, TL – tube lens, M – mirror, CM – curved focusing mirror, F_O – objective focal length, F_{TL} – tube lens focal length.

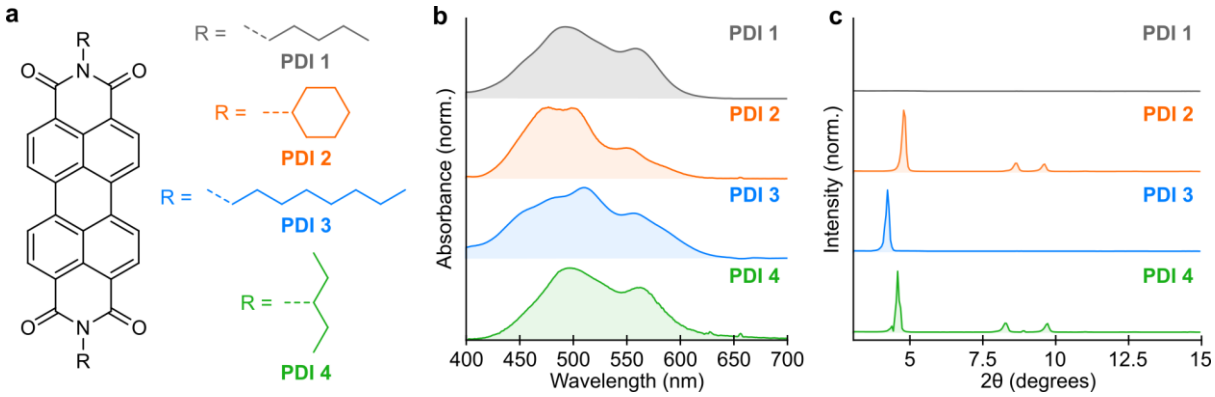

Figure 2. Characterization of evaporated perylene-diimide (PDI) thin films measured in this work. **a**. Chemical structure of PDI with various imide substituents termed **PDI 1 – 4**. **b**. Absorption spectra and **c**. X-Ray diffractograms of **PDI 1 – 4**. The degree of crystallinity increases in the order **PDI 1** to **PDI 4**, which is assessed by broadening of any diffraction peaks and atomic force microscopy characterization of the domain size (supplementary information, section 1 and section 5).

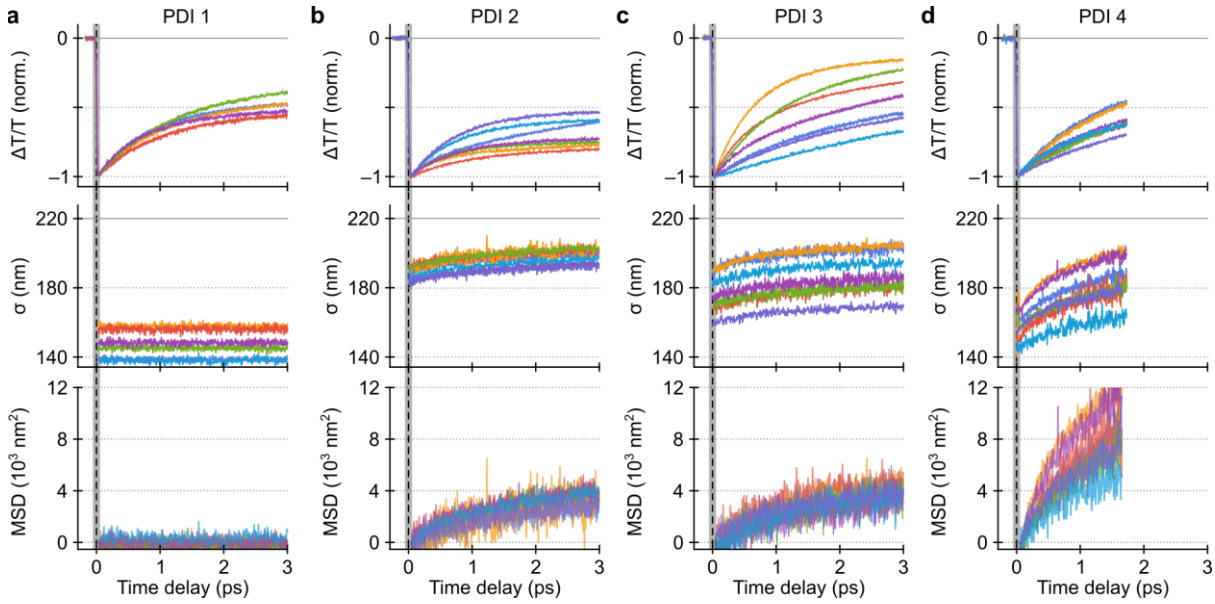

Figure 3. Femtosecond transient absorption microscopy results for studied the PDI films. **a-d.** Normalized transient absorption kinetics (top) and associated spatial dynamics (middle) recorded at 740 nm retrieved from an 2D Gaussian fit analysis. (bottom) Resulting time-dependent mean-square displacement curves (MSD). Individual color indicate experiments conducted different sample locations. The dashed black lines in the MSD curves represents a sub-diffusive transport fit (Equation 7). All pixels contributing to the to ΔT/T signal are averaged to obtain the kinetic. Scale bar – 500 nm.

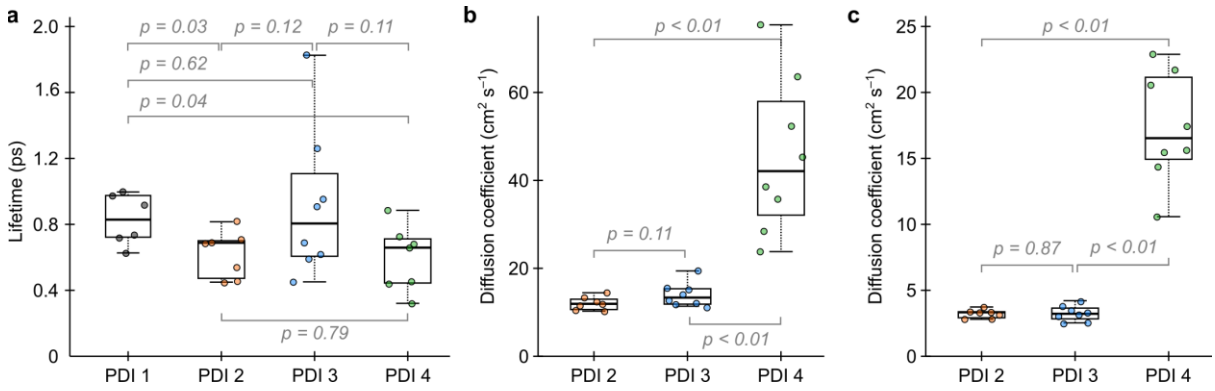

Figure 4. Retrieved spatio-temporal parameters PDI films. **a.** Box-plot representation of the fast component of the transient absorption kinetics. **b-c.** Box-plot representation of the retrieved diffusion coefficient in different time segments according to Equation 6 for PDI films that show transport (see main text for temporal segmentation). *p*-values according to a two-tailed Student *t*-test are indicated between each data set (grey).

Table 1. Overview of extracted parameters for PDI films studied in this work.

	PDI 1	**PDI 2**	**PDI 3**	**PDI 4**
Average grain Size (nm)	~20	~120	~120	>1000
D_1 (cm^2 s^{-1})	0 ± 0.7	11.9 ± 1.5	13.9 ± 2.7	45.3 ± 17.6
D_2 (cm^2 s^{-1})	0 ± 0.7	3.2 ± 0.3	3.3 ± 0.6	17.3 ± 4.1
L_1 (nm)	~0	15.4 ± 1.0	16.6 ± 1.6	30.1 ± 5.8

ASSOCIATED CONTENT

Supporting Information. AFM image analysis, carrier-concentration dependence, point-spread function analysis, Scherrer analysis, sub-diffusive fit results. This information is available free of charge via the Internet at http://pubs.acs.org.

The data underlying this work is available free of charge at [URL to be added in proof]

Corresponding Authors

*Christoph Schnedermann cs2002@cam.ac.uk

Akshay Rao ar525@cam.ac.uk

Author Contributions

The manuscript was written through contributions of all authors. All authors have given approval to the final version of the manuscript.

Acknowledgements

The research leading to these results has received funding from the European Research Council (ERC) under the European Union's Horizon 2020 research and innovation program (grant agreement no. 670405 and 758826). We acknowledge financial support from the EPSRC and the Winton Program for the Physics of Sustainability. C.S. acknowledges financial support by the Royal Commission of the Exhibition of 1851.

REFERENCES

(1) Ho, P. K. H.; Kim, J. I. S.; Burroughes, J. H.; Becker, H.; Li, S. F. Y.; Brown, T. M.; Cacialli, F.; Friend, R. H. Molecular-Scale Interface Engineering for Polymer Light-Emitting Diodes. *Nature* **2000**, *404*, 481–484.

(2) Matsushima, T.; Bencheikh, F.; Komino, T.; Leyden, M. R.; Sandanayaka, A. S. D.; Qin, C.; Adachi, C. High Performance from Extraordinarily Thick Organic Light-Emitting Diodes. *Nature* **2019**, *572*, 502–506.

(3) Yu, G.; Gao, J.; Hummelen, J. C.; Wudl, F.; Heeger, A. J. Polymer Photovoltaic Cells: Enhanced Efficiencies via a Network of Internal Donor-Acceptor Heterojunctions. *Science (80-.).* **1995**, *270* (5243), 1789–1791.

(4) Sirringhaus, H.; Tessler, N.; Friend, R. H. Integrated Optoelectronic Devices Based on Conjugated Polymers. *Science (80-.).* **1998**, *280* (5370), 1741–1744.

(5) Hendsbee, A. D.; Sun, J. P.; Law, W. K.; Yan, H.; Hill, I. G.; Spasyuk, D. M.; Welch, G. C. Synthesis, Self-Assembly, and Solar Cell Performance of N-Annulated Perylene Diimide Non-Fullerene Acceptors. *Chem. Mater.* **2016**, *28* (19), 7098–7109.

(6) Ryan, S. T. J.; Young, R. M.; Henkelis, J. J.; Hafezi, N.; Vermeulen, N. A.; Hennig, A.; Dale, E. J.; Wu, Y.; Krzyaniak, M. D.; Fox, A.; et al. Energy and Electron Transfer Dynamics within a Series of Perylene Diimide/Cyclophane Systems. *J. Am. Chem. Soc.* **2015**, *137* (48), 15299–15307.

(7) Pandya, R.; MacQueen, R. W.; Rao, A.; Davis, N. J. L. K. Simple and Robust Panchromatic Light Harvesting Antenna Composites via FRET Engineering in Solid State Host Matrices.

J. Phys. Chem. C **2018**, *122* (9), 22330–22338.

(8) Ogawa, S. *Organic Electronics Materials and Devices*; 2015.

(9) Akselrod, G. M.; Deotare, P. B.; Thompson, N. J.; Lee, J.; Tisdale, W. A.; Baldo, M. A.; Menon, V. M.; Bulović, V. Visualization of Exciton Transport in Ordered and Disordered Molecular Solids. *Nat. Commun.* **2014**, *5* (1), 3646.

(10) Caram, J. R.; Doria, S.; Eisele, D. M.; Freyria, F. S.; Sinclair, T. S.; Rebentrost, P.; Lloyd, S.; Bawendi, M. G. Room-Temperature Micron-Scale Exciton Migration in a Stabilized Emissive Molecular Aggregate. *Nano Lett.* **2016**, *16* (11), 6808–6815.

(11) Clark, K. A.; Krueger, E. L.; Vanden Bout, D. A. Direct Measurement of Energy Migration in Supramolecular Carbocyanine Dye Nanotubes. *J. Phys. Chem. Lett.* **2014**, *5* (13), 2274–2282.

(12) Haedler, A. T.; Kreger, K.; Issac, A.; Wittmann, B.; Kivala, M.; Hammer, N.; Köhler, J.; Schmidt, H. W.; Hildner, R. Long-Range Energy Transport in Single Supramolecular Nanofibres at Room Temperature. *Nature* **2015**, *523*, 196–199.

(13) Marciniak, H.; Li, X. Q.; Würthner, F.; Lochbrunner, S. One-Dimensional Exciton Diffusion in Perylene Bisimide Aggregates. *J. Phys. Chem. A* **2011**, *115* (5), 648–654.

(14) Lin, H.; Camacho, R.; Tian, Y.; Kaiser, T. E.; Würthner, F.; Scheblykin, I. G. Collective Fluorescence Blinking in Linear J-Aggregates Assisted by Long-Distance Exciton Migration. *Nano Lett.* **2010**, *10* (2), 620–626.

(15) Wong, C. Y.; Cotts, B. L.; Wu, H.; Ginsberg, N. S. Exciton Dynamics Reveal Aggregates with Intermolecular Order at Hidden Interfaces in Solution-Cast Organic Semiconducting

Films. *Nat. Commun.* **2015**, *6*, 5946.

(16) Menke, S. M.; Holmes, R. J. Exciton Diffusion in Organic Photovoltaic Cells. *Energy Environ. Sci.* **2014**, *7* (2), 499–512.

(17) Bardeen, C. J. The Structure and Dynamics of Molecular Excitons. *Annu. Rev. Phys. Chem.* **2014**, *65*, 127–148.

(18) Mikhnenko, O. V.; Blom, P. W. M.; Nguyen, T. Q. Exciton Diffusion in Organic Semiconductors. *Energy Environ. Sci.* **2015**, *8*, 1867–1888.

(19) Zhu, T.; Wan, Y.; Huang, L. Direct Imaging of Frenkel Exciton Transport by Ultrafast Microscopy. *Acc. Chem. Res.* **2017**, *50* (7), 1725–1733.

(20) Nah, S.; Spokoyny, B. M.; Soe, C. M. M.; Stoumpos, C. C.; Kanatzidis, M. G.; Harel, E. Ultrafast Imaging of Carrier Cooling in Metal Halide Perovskite Thin Films. *Nano Lett.* **2018**, *18* (2), 1044–1048.

(21) Massaro, E. S.; Hill, A. H.; Grumstrup, E. M. Super-Resolution Structured Pump-Probe Microscopy. *ACS Photonics* **2016**, *3* (4), 501–506.

(22) Fischer, M. C.; Wilson, J. W.; Robles, F. E.; Warren, W. S. Invited Review Article: Pump-Probe Microscopy. *Rev. Sci. Instrum.* **2016**, *87* (3), 031101.

(23) Hartland, G. V. Ultrafast Studies of Single Semiconductor and Metal Nanostructures through Transient Absorption Microscopy. *Chem. Sci.* **2010**, *1* (3), 303.

(24) Jones, C. A., Keans, N. M., Ho, J., Flach, J. T., Zanni, M. T. Impact of Non-Equilibrium Molecular Packings on Singlet Fission in Microcrystals Observed Using 2D White-Light

Microscopy. *Nat. Chem.* **2020**, *12*, 40–47.

(25) Zhu, T.; Huang, L. Exciton Transport in Singlet Fission Materials: A New Hare and Tortoise Story. *J. Phys. Chem. Lett.* **2018**, *9* (22), 6502–6510.

(26) Schnedermann, C.; Sung, J.; Pandya, R.; Verma, S. D.; Chen, R. Y. S.; Gauriot, N.; Bretscher, H. M.; Kukura, P.; Rao, A. Ultrafast Tracking of Exciton and Charge Carrier Transport in Optoelectronic Materials on the Nanometer Scale. *J. Phys. Chem. Lett.* **2019**, 6727–6733.

(27) Sung, J.; Schnedermann, C.; Ni, L.; Sadhanala, A.; Chen, R. Y. S.; Cho, C.; Priest, L.; Lim, J. M.; Kim, H.-K.; Monserrat, B.; et al. Long-Range Ballistic Propagation of Carriers in Methylammonium Lead Iodide Perovskite Thin Films. *Nat. Phys.* **2020**, *16* (2), 171–176.

(28) Schnedermann, C.; Lim, J. M.; Wende, T.; Duarte, A. S.; Ni, L.; Gu, Q.; Sadhanala, A.; Rao, A.; Kukura, P. Sub-10 Fs Time-Resolved Vibronic Optical Microscopy. *J. Phys. Chem. Lett.* **2016**, *7* (23), 4854–4859.

(29) Che, Y.; Yang, X.; Balakrishnan, K.; Zuo, J.; Zang, L. Highly Polarized and Self-Waveguided Emission from Single-Crystalline Organic Nanobelts. *Chem. Mater.* **2009**, *21* (13), 2930–2934.

(30) Würthner, F.; Kaiser, T. E.; Saha-Möller, C. R. J-Aggregates: From Serendipitous Discovery to Supramolecular Engineering of Functional Dye Materials. *Angew. Chemie - Int. Ed.* **2011**, *50* (15), 3376–3410.

(31) Wang, H.; Kaiser, T. E.; Uemura, S.; Würthner, F. Perylene Bisimide J-Aggregates with Absorption Maxima in the NIR. *Chem. Commun.* **2008**, 1181–1183.

(32) Percec, V.; Peterca, M.; Tadjiev, T.; Zeng, X.; Ungar, G.; Leowanawat, P.; Aqad, E.; Imam, M. R.; Rosen, B. M.; Akbey, U.; et al. Self-Assembly of Dendronized Perylene Bisimides into Complex Helical Columns. *J. Am. Chem. Soc.* **2011**, *133* (31), 1297–12219.

(33) Gorman, J.; Pandya, R.; Allardice, J. R.; Price, M. B.; Schmidt, T. W.; Friend, R. H.; Rao, A.; Davis, N. J. L. K. Excimer Formation in Carboxylic Acid-Functionalized Perylene Diimides Attached to Silicon Dioxide Nanoparticles. *J. Phys. Chem. C* **2019**, *123* (6), 3433–3449.

(34) Malenfant, P. R. L.; Dimitrakopoulos, C. D.; Gelorme, J. D.; Kosbar, L. L.; Graham, T. O.; Curioni, A.; Andreoni, W. N-Type Organic Thin-Film Transistor with High Field-Effect Mobility Based on a N,N′-Dialkyl-3,4,9,10-Perylene Tetracarboxylic Diimide Derivative. *Appl. Phys. Lett.* **2002**, *80* (2517).

(35) Zhang, X.; Lu, Z.; Ye, L.; Zhan, C.; Hou, J.; Zhang, S.; Jiang, B.; Zhao, Y.; Huang, J.; Zhang, S.; et al. A Potential Perylene Diimide Dimer-Based Acceptor Material for Highly Efficient Solution-Processed Non-Fullerene Organic Solar Cells with 4.03% Efficiency. *Adv. Mater.* **2013**, *25*, 5791–5797.

(36) Zhong, Y.; Trinh, M. T.; Chen, R.; Wang, W.; Khlyabich, P. P.; Kumar, B.; Xu, Q.; Nam, C. Y.; Sfeir, M. Y.; Black, C.; et al. Efficient Organic Solar Cells with Helical Perylene Diimide Electron Acceptors. *J. Am. Chem. Soc.* **2014**, *136* (43), 15215–15221.

(37) Huang, Y.; Zhang, W.; Wang, J.; Wei, Z. Probing the Sensory Property of Perylenediimide Derivatives in Hydrazine Gas: Core-Substituted Aromatic Group Effect. *ACS Appl. Mater. Interfaces* **2014**, *6* (12), 9307–9313.

(38) Calzado, E. M.; Villalvilla, J. M.; Boj, P. G.; Quintana, J. A.; Gómez, R.; Segura, J. L.; Díaz-García, M. A. Effect of Structural Modifications in the Spectral and Laser Properties of Perylenediimide Derivatives. *J. Phys. Chem. C* **2007**, *111* (36), 13595–13605.

(39) Chaudhuri, D.; Li, D.; Che, Y.; Shafran, E.; Gerton, J. M.; Zang, L.; Lupton, J. M. Enhancing Long-Range Exciton Guiding in Molecular Nanowires by H-Aggregation Lifetime Engineering. *Nano Lett.* **2011**, *11* (2), 488–492.

(40) Yang, Y.; Wang, Y.; Xie, Y.; Xiong, T.; Yuan, Z.; Zhang, Y.; Qian, S.; Xiao, Y. Fused Perylenebisimide–Carbazole: New Ladder Chromophores with Enhanced Third-Order Nonlinear Optical Activities. *Chem. Commun.* **2011**, *47* (38), 10749.

(41) Davydova, D.; de la Cadena, A.; Akimov, D.; Dietzek, B. Transient Absorption Microscopy: Advances in Chemical Imaging of Photoinduced Dynamics. *Laser Photon. Rev.* **2016**, *10* (1), 62–81.

(42) Le, A. K.; Bender, J. A.; Roberts, S. T. Slow Singlet Fission Observed in a Polycrystalline Perylenediimide Thin Film. *J. Phys. Chem. Lett.* **2016**, *7* (23), 4922–4928.

(43) Le, A. K.; Bender, J. A.; Arias, D. H.; Cotton, D. E.; Johnson, J. C.; Roberts, S. T. Singlet Fission Involves an Interplay between Energetic Driving Force and Electronic Coupling in Perylenediimide Films. *J. Am. Chem. Soc.* **2018**, *140* (2), 814–826.

(44) Yagai, S.; Seki, T.; Karatsu, T.; Kitamura, A.; Würthner, F. Transformation from H- to J-Aggregated Perylene Bisimide Dyes by Complexation with Cyanurates. *Angew. Chemie - Int. Ed.* **2008**, *47*, 3367 –3371.

(45) Chen, Z.; Baumeister, U.; Tschierske, C.; Würthner, F. Effect of Core Twisting on Self-

Assembly and Optical Properties of Perylene Bisimide Dyes in Solution and Columnar Liquid Crystalline Phases. *Chem. - A Eur. J.* **2007**, *13*, 450–465.

(46) Tian, Y.; Stepanenko, V.; Kaiser, T. E.; Würthner, F.; Scheblykin, I. G. Reorganization of Perylene Bisimide J-Aggregates: From Delocalized Collective to Localized Individual Excitations. *Nanoscale* **2012**, *4*, 218–223.

(47) Hestand, N. J.; Spano, F. C. Molecular Aggregate Photophysics beyond the Kasha Model: Novel Design Principles for Organic Materials. *Acc. Chem. Res.* **2017**, *50* (2), 341–350.

(48) Grumstrup, E. M. Spatiotemporal Coupling of Excited State Dynamics in Time-Resolved Microscopies. *Opt. Express* **2019**, *27* (22), 31385.

(49) Kennehan, E. R.; Grieco, C.; Brigeman, A. N.; Doucette, G. S.; Rimshaw, A.; Bisgaier, K.; Giebink, N. C.; Asbury, J. B. Using Molecular Vibrations to Probe Exciton Delocalization in Films of Perylene Diimides with Ultrafast Mid-IR Spectroscopy. *Phys. Chem. Chem. Phys.* **2017**, *19*, 24829–24839.

(50) Clark, J.; Chang, J. F.; Spano, F. C.; Friend, R. H.; Silva, C. Determining Exciton Bandwidth and Film Microstructure in Polythiophene Films Using Linear Absorption Spectroscopy. *Appl. Phys. Lett.* **2009**, *163306*.

(51) Schierl, C.; Niazov-Elkan, A.; Shimon, L. J. W.; Feldman, Y.; Rybtchinski, B.; Guldi, D. M. Singlet Fission in Self-Assembled PDI Nanocrystals. *Nanoscale* **2018**, *10*, 20147–20154.

(52) Felter, K. M.; Caselli, V. M.; Günbaş, D. D.; Savenije, T. J.; Grozema, F. C. Interplay between Charge Carrier Mobility, Exciton Diffusion, Crystal Packing, and Charge

Separation in Perylene Diimide-Based Heterojunctions. *ACS Appl. Energy Mater.* **2019**, *2* (11), 8010–8021.

(53) Jin, X.-H.; Price, M. B.; Finnegan, J. R.; Boott, C. E.; Richter, J. M.; Rao, A.; Menke, S. M.; Friend, R. H.; Whittell, G. R.; Manners, I. Long-Range Exciton Transport in Conjugated Polymer Nanofibers Prepared by Seeded Growth. *Science (80-.).* **2018**, *360* (6391), 897–900.

(54) Brixner, T.; Hildner, R.; Köhler, J.; Lambert, C.; Würthner, F. Exciton Transport in Molecular Aggregates - From Natural Antennas to Synthetic Chromophore Systems. *Adv. Energy Mater.* **2017**, *7* (16), 1700236.

(55) Malý, P.; Lüttig, J.; Turkin, A.; Dostál, J.; Lambert, C.; Brixner, T. From Wavelike to Sub-Diffusive Motion : Exciton Dynamics and Interaction in Squaraine Copolymers of Varying Length. *Chem. Sci.* **2019**, *11*, 456–466.

(56) Sung, J.; Kim, P.; Fimmel, B.; Würthner, F.; Kim, D. Direct Observation of Ultrafast Coherent Exciton Dynamics in Helical π-Stacks of Self-Assembled Perylene Bisimides. *Nat. Commun.* **2015**, *6* (1), 8646.

(57) Lebedenko, A. N.; Guralchuk, G. Y.; Sorokin, A. V.; Yeflmova, S. L.; Malyukin, Y. V. Pseudoisocyanine J-Aggregate to Optical Waveguiding Crystallite Transition: Microscopic and Microspectroscopic Exploration. *J. Phys. Chem. B* **2006**, *110* (36), 17772–17775.

TOC Graphic

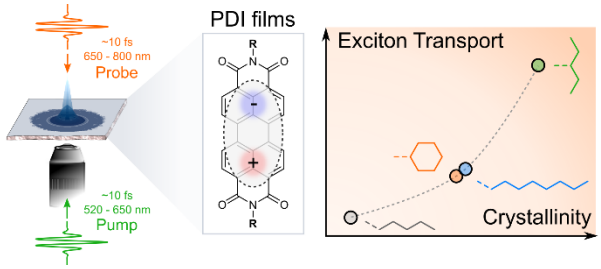
~10 fs
650 - 800 nm
Probe
~10 fs
520 - 650 nm
Pump
PDI films
Exciton Transport
Crystallinity